Available online at www.sciencedirect.com
SCIENCE DIRECT®
Journal of Hydrology 274 (2003) 176–197
Journal of Hydrology
www.elsevier.com/locate/jhydrol

A new visualization technique for the study of solute dispersion in model porous media

M.A. Theodoropoulou[a,b], V. Karoutsos[a], C. Kaspiris[c], C.D. Tsakiroglou[a,*]

[a]*Institute of Chemical Engineering and High Temperature Chemical Processes, Foundation for Research and Technology Hellas Stadiou Street, Platani, P.O. Box 1414, GR-26504 Patras, Greece*
[b]*Department of Pharmacy, University of Patras, GR-26504 Patras, Greece*
[c]*Department of Electrical and Computer Engineering, University of Patras, GR-26504 Patras, Greece*

Received 8 May 2002; revised 25 November 2002; accepted 29 November 2002

Abstract

A new technique of high resolution is developed to perform visualization experiments of the hydrodynamic dispersion of pollutants in transparent glass-etched pore networks, which are regarded as representative models of natural porous media and single fractures. The technique is based on the continuous detection of the sharp colour changes caused on an aqueous solution, as the solute concentration varies, because of the strong sensitivity of a system of indicators to pH. Image analysis is used for the transformation of the spatial distribution of colour intensity to solute concentration profiles. Unidirectional miscible displacement and single source-solute transport experiments are used to identify and quantify the transient and steady-state solute dispersion regimes in a pore network, and estimate the longitudinal and transverse dispersion coefficients as functions of Peclet number. The dispersion coefficients are estimated by fitting the spatial/temporal distribution of solute concentration over various regions of the network to analytic solutions of the convection–dispersion equation, obtained by using a flux-type boundary condition at solute sources. The experimental technique and the method of analysis of its results may be proved very useful for model validation, sensitivity analysis of dispersion coefficients with respect to pore space parameters, and identification of liquid pollutant dispersion regimes in underground aquifers.

Keywords: Pore network; Dispersion coefficients; Peclet number; Parameter estimation; Image analysis; Solute dispersion

1. Introduction

Non-aqueous phase liquids (NAPLs) may contaminate underground aquifers by a variety of fluid transport mechanisms among which, the dissolution of NAPL compounds (solute) in the flowing aqueous phase (solvent) and the consequent dispersion of dissolved NAPL at long distances within the reservoir have received considerable attention (Bear et al., 1993). In general, the hydrodynamic dispersion can be viewed as the spreading of a tracer carried along by a flowing fluid in a porous medium of disordered structure. Dispersion is driven by the interplay of fluid motion (convection) and molecular diffusion in the pore space (Taylor, 1953; Aris, 1956). Dispersion processes play an important role in a wide variety of environmental and technological processes (Sahimi, 1995), such as the pollutant spreading in groundwater

* Corresponding author. Tel.: +30-2610-965212; fax: +30-2610-965223.
E-mail address: ctsakir@iceht.forth.gr (C.D. Tsakiroglou).

0022-1694/03/$ - see front matter © 2003 Elsevier Science B.V. All rights reserved.
doi:10.1016/S0022-1694(02)00421-3

and clean-up of contaminated sites, secondary oil recovery operations, separation processes such as chromatography, catalytic processes, degradation of building materials, etc.

Solute dispersion in a porous medium arises from spatial fluctuations of the velocity field, which, in turn, are governed by the chaotic nature of the pore space morphology (Sahimi et al., 1986). A great deal of experimental work has been focused on the determination of the hydrodynamic dispersion coefficients as function of the Peclet number by using a variety of techniques (acoustic, NMR, CT-Scan, radioactive tracers, etc.) for the measurement of the transient changes of solute concentration (Sahimi, 1995; Bacri et al., 1987; Ding and Candela, 1996; Peters et al., 1996; Drazer et al., 1999; Manz et al., 1999). On the other hand, the numerical calculation of dispersion coefficients in porous media has been based on pore network simulations (Sahimi et al., 1986; de Arcangelis et al., 1986; Oppenheimer, 2000; Bruderer and Bernabe, 2001), Lattice-Boltzman algorithms (Lowe and Frenkel, 1996; Drazer and Koplik, 2001), volume averaging and solution of the corresponding closure problems in spatially periodic unit cells (Souto and Moyne, 1997; Whitaker, 1999; Ahmadi et al., 2001), method of moments (Huseby et al., 2001), etc. In general, the dispersion coefficients have been found to be non-linear functions of Peclet number, and five dispersion regimes have roughly been distinguished depending on the prevailing transport mechanism (Sahimi, 1995): (i) the diffusion regime ($Pe < 0.3$), (ii) the transition regime ($0.3 < Pe < 5$), (iii) the power law regime ($5 < Pe < 300$), (iv) the pure convection or mechanical dispersion regime ($300 < Pe < 10^5$), and (v) the turbulent dispersion regime ($Pe > 10^5$). In addition, there is experimental and theoretical evidence about the fractal character of the solute concentration contours and the scale-dependence of hydrodynamic dispersion in two-dimensional (2D) porous media (Maloy et al., 1988; Martys, 1994; Birovljev et al., 1994), though no generalized dispersion scaling law has yet been deduced.

The dispersion of dissolved contaminants in fractured rocks and soils (Adler and Thovert, 1999) depends strongly on the variability of the fracture aperture, and large fracture aperture regions result in significant channelling of the fluid flow. Recent studies have revealed that the fracture aperture in many types of fractured media can successfully be represented by a 2D disordered network of elliptical channels (Klint and Tsakiroglou, 2000). Results of field (Shapiro and Nicholas, 1989) and laboratory (Neretnieks et al., 1982) experiments as well as theoretical investigations (Johns and Roberts, 1991) suggest that the variability of fracture aperture plays an important role on solute dispersion: fluid flow appears to be channelled, primarily through large aperture regions of the fracture that comprise only a small percentage of the fracture active area (Keller et al., 1998).

Visualization dispersion experiments performed on transparent model porous media of regular morphology (Charlaix et al., 1988; Corapcioglu et al., 1997; Didierjean et al., 1997) and artificial fractures (Detwiller et al., 2000) are useful not only for the quantification of the dispersion coefficients as functions of Peclet number and structural properties of the pore space, but also for the identification of the dispersion flow regimes, the understanding of small-scale effects on the macroscopic coefficients and the evaluation of models and numerical simulators.

In the present work, a new technique is developed to perform high resolution visualization experiments of solute (HCl) dispersion on artificial glass-etched planar pore networks which can be regarded as representative models of the porous matrix or single fractures in natural formations. The temporal and spatial evolution of solute concentration distribution throughout the pore network is measured by using image analysis. The contours of equal solute concentration are determined for two types of transient experiments: (i) miscible displacement of a dilute HCl solution by a dense one, and (ii) steady injection of a dense HCl solution through a single source into a dilute HCl solution flowing through the pore network. The transient and steady-state HCl concentration profiles are fitted to analytic solutions of the macroscopic convection–dispersion equation so that the longitudinal and transverse dispersion coefficients are estimated as functions of Peclet number.

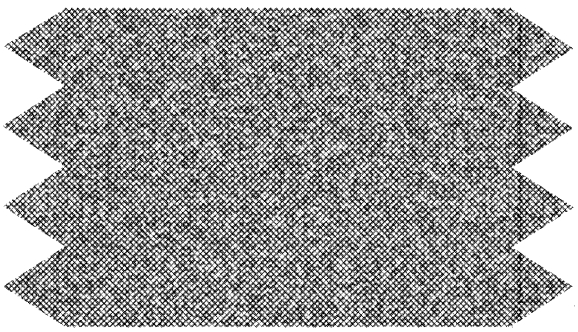

Model M-1

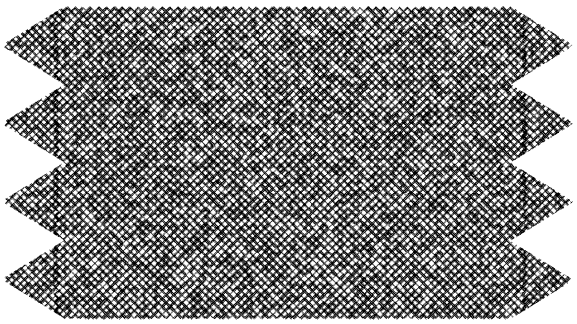

Model: M-2

Fig. 1. Patterns of model porous media used in experiments.

2. Materials and methods

2.1. Experimental set-up

Photolithography was used to fabricate artificial large 2D pore networks by etching mirror image patterns (Fig. 1) on two glass plates with hydrofluoric acid, and sintering the pre-aligned etched plates in a programmable furnace. The pore cross-sectional shape in these models is lenticular (Tsakiroglou et al., 1997). The pore width distribution ($\langle W_P \rangle$, σ_W) was determined by estimating the relative variation caused on the pore sizes of patterns (Fig. 1) by the etching and sintering processes, whereas the pore depth distribution ($\langle D_P \rangle$, σ_D) was estimated with reference to earlier studies (Tsakiroglou and Payatakes, 1998) and by matching the calculated value of the absolute permeability to the experimentally measured one (Table 1). It is well known that hydrodynamic dispersion is affected by the variance of the pore size distribution and porosity (Bruderer and Bernabe, 2001; Adler and Thovert, 1999). For this reason, two pore network models, M-1 and M-2 (Fig. 1), differing in the mean value/standard deviation of the pore-width distribution and areal porosity, were fabricated (Table 1).

An experimental apparatus was constructed to perform visualization experiments of multi-phase flow on planar pore networks (Theodoropoulou et al., 2001). The entire system is placed in a cooled incubator (Fig. 2a) in order to keep constant temperature and avoid any undesired changes in fluid properties. The fluids are injected in the pore network through four inlet ports and expel from it through four outlet ports, whereas four other holes drilled on the centre of the network serve either as solute sources or as pressure taps (Fig. 2b). One or two syringe pumps are used for the injection of fluids, and a CCD camera, connected with an image

Table 1
Structural properties of model porous media

Property	Model M-1	Model M-2
Dimensions, width × length (inlet–outlet)	10.3 cm × 14.5 cm	10.3 cm × 14.5 cm
Topology	Square lattice	Square lattice
Pore orientation with respect to main flow	$\theta = 45°$	$\theta = 45°$
Areal porosity, ϕ_A	0.55	0.65
Total pore cross-sectional area, A_P (m^2)	5.1×10^{-6}	5.9×10^{-6}
Mean pore width, $\langle W_P \rangle$ (μm)	470	774
Standard deviation of pore width, σ_W (μm)	168	274
Mean pore depth, $\langle D_P \rangle$ (μm)	126	125
Standard deviation of pore depth, σ_D (μm)	20	20
Constant pore length, L_P (μm)	1365	1840
Absolute permeability, k (Da)	20.5	19.6

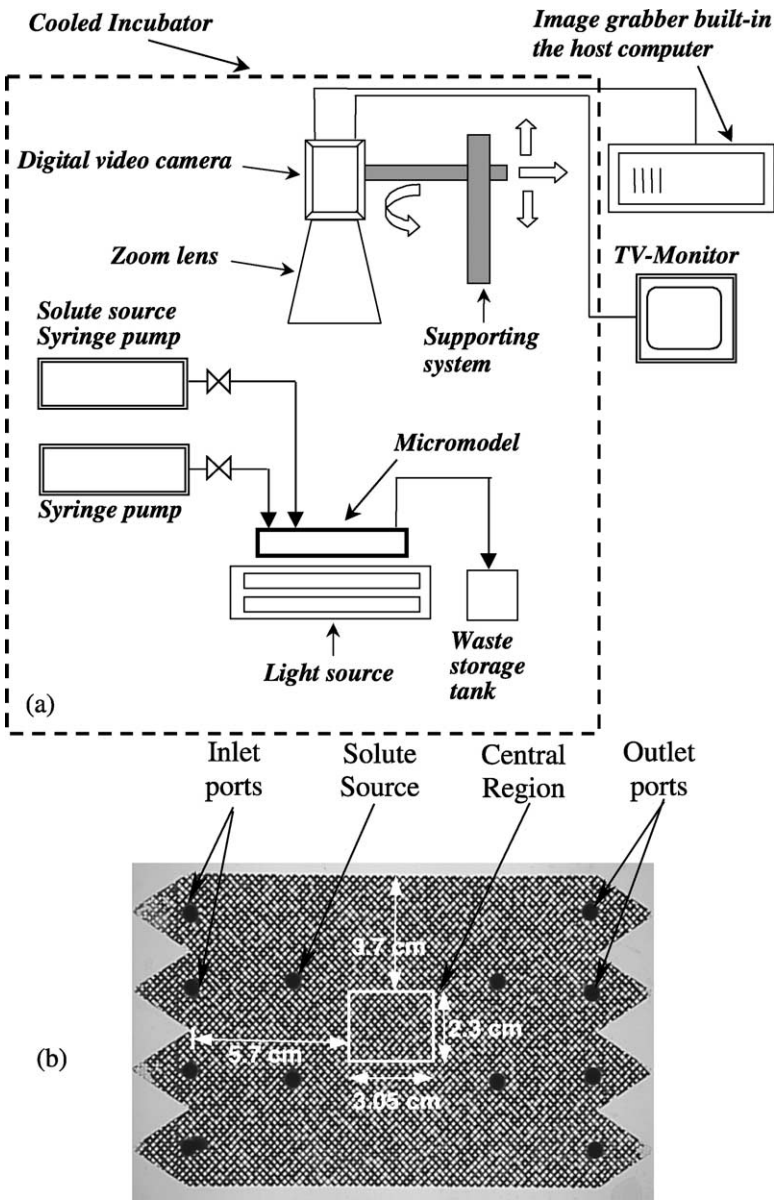

Fig. 2. (a) Schematic diagram of experimental set-up. (b) Artificial glass model.

grabber that is installed in a PC, is used to capture images and store them directly on the hard-disk of the PC (Fig. 2a). The model is illuminated by a transmitted light source placed beneath it. The light source is covered by a semi-transparent plate whereas the incubator is kept closed during experiments, so that conditions of uniform and identical light distribution over the glass surface are ensured.

A technique was developed for the measurement of the transient changes of the solute concentration distribution throughout the pore network. The technique is based on the detection of colour changes caused on a dilute HCl aqueous solution ($C = 0.03$

g mol/l) during its mixing with a dense HCl solution ($C = 0.43$ g mol/l). A system of organic indicators are contained in traces in both solutions. The colour of indicators is so sensitive to the pH of the solution that even a small change in solute concentration causes detectable changes in the colour intensity as described in detail below. Regarding the resolution of the technique, it's worthwhile noting that eighteen colours can be distinguished within the full range of solute concentrations used in experiments.

2.2. Hydrodynamic dispersion experiments

Two types of dispersion experiments were conducted: (a) miscible displacement experiments that were used to identify the transient dispersion regimes and measure the solute concentration distribution at a central region of the pore network (Figs. 2b and 3a), and (b) single source-solute transport experiments that were used to identify the steady-state dispersion regimes (Fig. 3b) and measure the transient changes of the solute concentration distribution at various regions of the pore network (Fig. 3c). In miscible displacement experiments, the artificial fracture was initially filled with the low HCl concentration solution, whereas the high HCl concentration solution was injected through four inlet ports of the model at a constant flow rate. Solute concentrations were measured within a small central region of the network (Figs. 2b and 3a). In single source-solute transport experiments, the dilute HCl solution was flowing steadily through the porous medium at a constant rate, Q, while the dense HCl solution was being injected continuously in a central hole of the artificial model, at a sufficiently low rate, Q_s, ($Q_s = 0.05Q$), ensuring that the flow field remained undisturbed. The solute concentration was measured in various regions downstream the source (Fig. 3b and c). In both types of experiments, successive images were recorded either from time to time (for low flow rates) or continuously (for high flow rates) and were stored on the hard-disk of PC for further analysis.

First, the relationship of the pH of the aqueous solution with HCl concentration was established

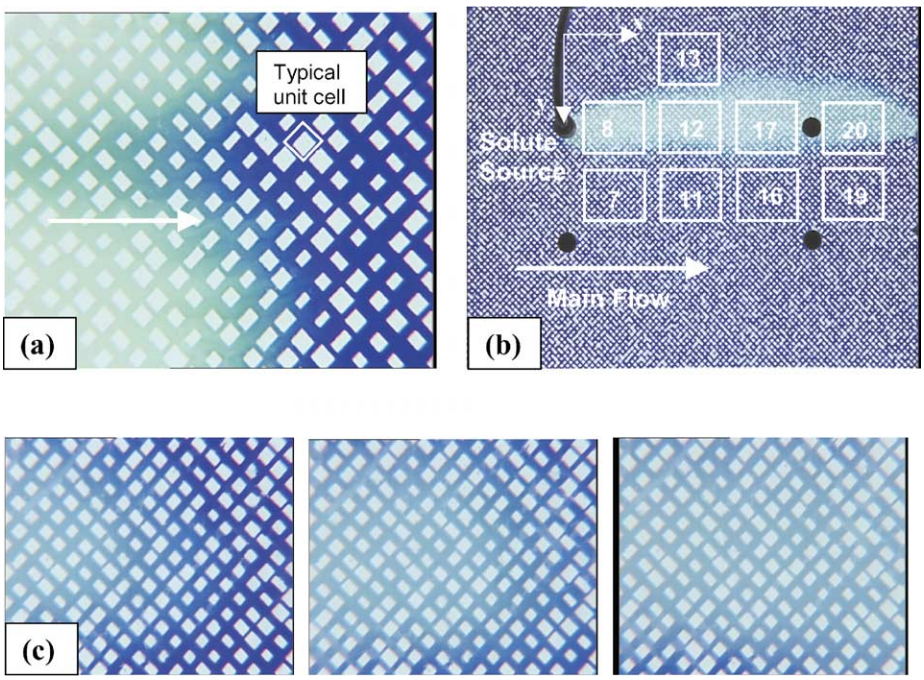

Fig. 3. (a) Short-cuts of the miscible displacement in the pore network of glass model M-2 ($Pe = 45.0$). (b) Steady-state dispersion regime ($Pe = 3.0$) for solute transport from a single source in the pore network of glass model M-1. (c) Successive pictures of the transient solute dispersion in the region 12 of (b) (the lighter the colour the higher the solute concentration).

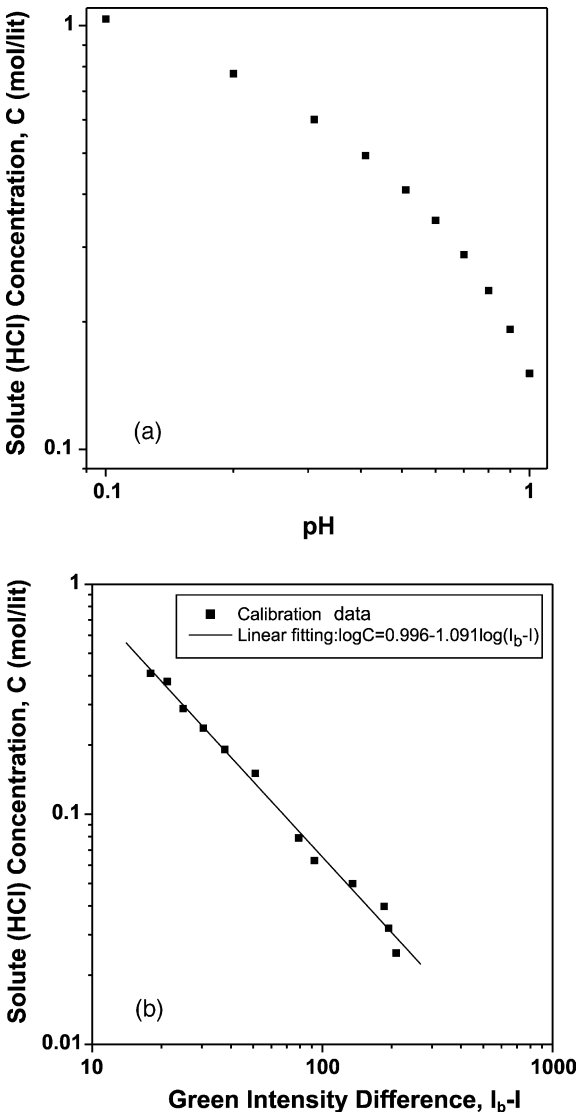

Fig. 4. (a) HCl concentration vs pH. (b) HCl concentration vs colour intensity difference.

(Fig. 4a) by using thermodynamic data concerning the ionic activity coefficient of HCl solutions (Robinson and Stokes, 1970). Then, calibration curves were constructed to relate the (intrinsic) local average HCl concentration, C, with the difference $I_b - I$, (Fig. 4b), where I_b is the local colour intensity averaged over the solid area (background) and I is the local colour intensity averaged over the pore area ($0 \leq I$, $I_b \leq 255$). Between green, red and blue colours, the green colour intensity (Fig. 3) was found to be the most sensitive to the solute concentration variation. Representative unit cells consisting of four interconnected pores in square arrangement (Fig. 3a) were regarded as the elementary units for the determination of the (intrinsic) local average solute concentrations. For the construction of calibration curves, the pore network was saturated with standard solutions of known HCl concentration, images of pre-specified regions of the network were captured with the aid of the camera and image grabber (Digitsuite Matrox), and the intrinsic average green colour intensity of individual unit cells was measured with the aid of Sigma Scan Pro 5.0 (SPSS) image analysis software. No important differences were found amongst calibration curves of the various unit cells so that an average curve was determined for each measured region of the pore network.

An efficient algorithm was developed in the environment of Scan Pro 5.0 (SPSS) for the automatic identification of the pore space and solid matrix, recognition of the boundaries of unit cells and measurement of the intrinsic average colour intensity of each unit cell over each region. Afterwards, with the aid of calibration curves, the colour intensities were converted to solute (HCl) concentrations.

3. Theoretical analysis

At a macroscopically homogeneous porous medium, the transient evolution of the spatial distribution of the solute concentration in it is obtained by volume averaging of the local component mass balances (Whitaker, 1999) which, for one-dimensional flow at constant velocity, is expressed by the well-known convection–dispersion equation

$$\frac{\partial C}{\partial t} + u_0 \frac{\partial C}{\partial x} = D_L \frac{\partial^2 C}{\partial x^2} + D_T \frac{\partial^2 C}{\partial y^2} \quad (1)$$

where C is the solute concentration, u_0 is the mean pore velocity, and D_L, D_T are the longitudinal and transverse dispersion coefficients, respectively. The 2D geometry of the aforementioned experiments is shown in Fig. 5a and c. In order to solve analytically the solute dispersion problem, we assume, in both cases, that (i) the porous medium extends to infinity

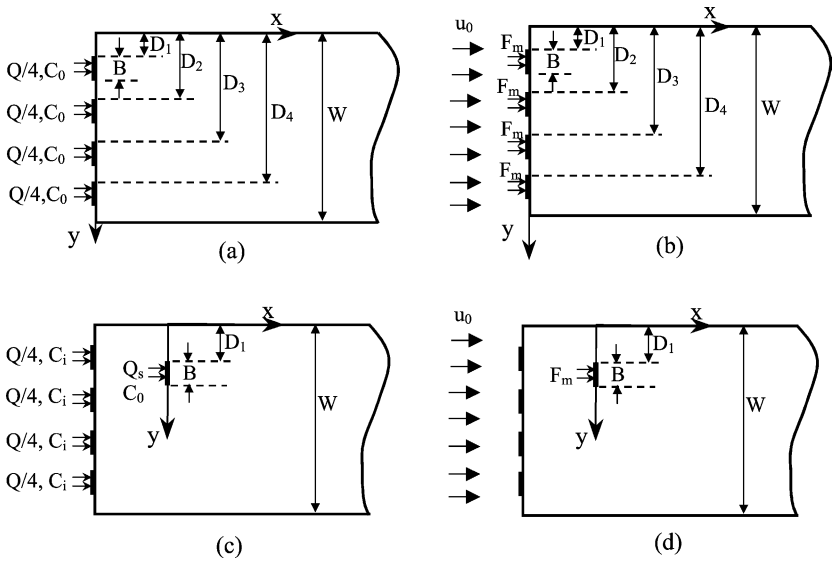

Fig. 5. Schematic representation of experiments and theoretical models. (a) Miscible displacement experiment. (b) Model of (a) with flux-type source inputs. (c) Single source-solute transport experiment. (d) Model of (c) with flux-type source input.

along the x-axis, (ii) the lateral boundaries are impervious, and (iii) a solution with solute concentration C_i flows at a constant axial pore velocity, u_0; at time $t = 0$, a solution with solute concentration, C_0, is injected at a uniform solute flux, F_m, through a single or multiple sources (Fig. 5b and d).

By defining the dimensionless solute concentration

$$C^* = (C - C_i)/(C_0 - C_i) \tag{2}$$

Eq. (1) remains unaltered if C is replaced with C^*. The local convective–dispersive fluxes are given by

$$F_x = (C_0 - C_i)\left(\phi u_0 C^* - \phi D_L \frac{\partial C^*}{\partial x}\right) \tag{3}$$

$$F_y = -\phi D_T (C_0 - C_i)\frac{\partial C^*}{\partial y} \tag{4}$$

and the flux-type boundary condition at the source is expressed by

$$F_m = (C_0 - C_i)\left[\phi u_0 C^* - \phi D_L \frac{\partial C^*}{\partial x}\right]_{x=0} \tag{5}$$

where ϕ is the porosity which is defined as the ratio of the pore cross-sectional area to the (reference) total cross-sectional area. Eq. (1) is solved analytically (Batu, 1993) by taking its Laplace transform, applying the method of variable separation, determining the inverse Laplace transform of the resulting equation, using the flux-type source (Gauchy) condition, Eq. (5), and considering that $\partial C/\partial x = 0$ at $x = \infty$. Finally it is obtained

$$\begin{aligned} C^*(x,y,t) = \frac{1}{C_0 - C_i}\Bigg\{ & \frac{2I_0}{WD_L}\int_0^t F_1(\xi)[F_2(\xi) \\ & - F_3(\xi)F_4(\xi)]\mathrm{d}\xi \\ & + \frac{2}{WD_L}\sum_{n=1}^{\infty} I_n \cos(\lambda_n y) \\ & \int_0^t F_1(\xi)\exp(-D_T\lambda_n^2\xi)[F_2(\xi) \\ & - F_3(\xi)F_4(\xi)]\mathrm{d}\xi\Bigg\} \end{aligned} \tag{6}$$

where

$$\lambda_n = \frac{n\pi}{W} \tag{7}$$

$$F_1(\xi) = \exp\left(\frac{u_0 x}{2D_L} - \frac{u_0^2\xi}{4D_L}\right) \tag{8}$$

$$F_2(\xi) = \left(\frac{D_L}{\pi\xi}\right)^{1/2}\exp\left(-\frac{x^2}{4D_L\xi}\right) \tag{9}$$

$$F_3(\xi) = \frac{u_0}{2}\exp\left(\frac{u_0^2\xi}{4D_L} + \frac{u_0 x}{2D_L}\right) \tag{10}$$

$$F_4(\xi) = \mathrm{erfc}\left[\frac{u_0}{2}\left(\frac{\xi}{D_L}\right)^{1/2} + \frac{x}{2(D_L\xi)^{1/2}}\right] \tag{11}$$

$$I_0 = \int_0^W \frac{F_m}{\phi}\mathrm{d}y \tag{12}$$

$$I_n = \int_0^W \frac{F_m}{\phi}\cos(\lambda_n y)\mathrm{d}y \tag{13}$$

In single source-solute transport experiments (Fig. 5c), the flow field has fully been developed before the flowing solution of concentration C_i reaching the source. In addition, the flow field is not disturbed sensibly by the injected solution of concentration C_0 ($Q_s \ll Q$), and hence the assumption (iii) is not far from reality (Fig. 5d). In miscible displacement experiments (Fig. 5a), no main flow field pre-exists, and the flow is fully developed at a certain axial distance from inlet ports (Fig. 5a). Therefore, the hydrodynamic problem (Fig. 5a) has to be solved in order to evaluate the simplified approach of the solute dispersion problem (Fig. 5b). The flow field (Fig. 5a) is determined by solving the steady-state continuity equation

$$\frac{\partial u_x}{\partial x} + \frac{\partial u_y}{\partial y} = 0 \tag{14}$$

with the boundary conditions

$$u_y = 0 \qquad \text{at } y = 0 \text{ and } y = W \tag{15}$$

$$u_x = u_s = \frac{Q}{\phi B L_P} \tag{16}$$

$$\text{at } D_j \le y \le D_j + B, \quad j = 1,2,3,4$$

$$u_x = u_\infty = \frac{Q}{A_P} \qquad \text{as } x \to \infty \tag{17}$$

where u_s is the x-component of the pore velocity at the sources (inlet ports), u_∞ is its asymptotic value at large distances from the entrance and A_P is the total pore cross-sectional area. The x-, y-components of the average intrinsic (pore) flow velocity, u_x and u_y are given by Darcy's law, namely

$$u_x = \frac{k}{\varphi\mu}\left(-\frac{\partial P}{\partial x}\right) \tag{18}$$

$$u_y = \frac{k}{\varphi\mu}\left(-\frac{\partial P}{\partial y}\right) \tag{19}$$

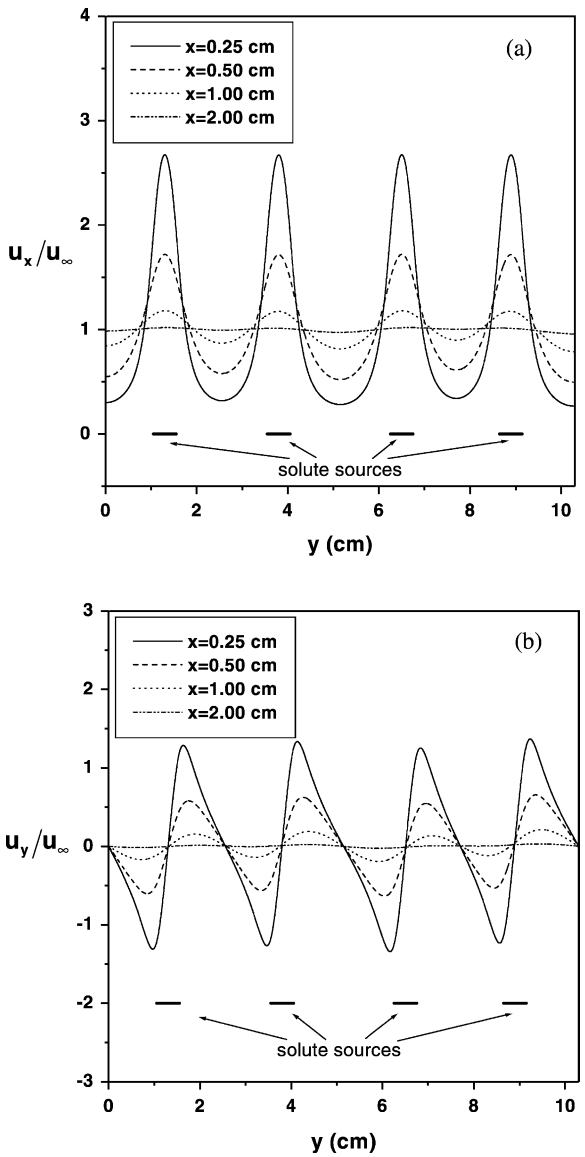

Fig. 6. Flow velocity profiles of multi-source miscible displacement experiments, calculated with Eqs. (20) and (21). (a) Dimensionless x-component of flow velocity. (b) Dimensionless y-component of flow velocity.

where k is the permeability of the porous medium, and μ is the fluid viscosity. By introducing Eqs. (18) and (19) into Eq. (14) and solving the resulting equation with variable separation and expansion in Fourier series, we get

$$u_x(x,y) = u_\infty + \sum_{n=1}^{\infty} \frac{2u_s}{\lambda_n W} \exp(-\lambda_n x) A_n \cos(\lambda_n y) \quad (20)$$

$$u_y(x,y) = \sum_{n=1}^{\infty} \frac{2u_s}{\lambda_n W} \exp(-\lambda_n x) A_n \sin(\lambda_n y) \quad (21)$$

where

$$\begin{aligned} A_n = \{&[\sin[\lambda_n(D_1 + B)] - \sin(\lambda_n D_1)] \\ &+ [\sin[\lambda_n(D_2 + B)] - \sin(\lambda_n D_2)] \\ &+ [\sin[\lambda_n(D_3 + B)] - \sin(\lambda_n D_3)] \\ &+ [\sin[\lambda_n(D_4 + B)] - \sin(\lambda_n D_4)]\} \end{aligned} \quad (22)$$

The flow velocity profiles across y-axis, at different axial positions in the pore network M-2 (Table 1), are shown in Fig. 6a and b. Obviously, the assumption of constant axial pore velocity (Fig. 5b) fails near solute sources ($x < 2$ cm). However, the hydrodynamic dispersion tensor originates from the spatial deviations of the local flow velocity vector and local solute concentration from their average values (Whitaker, 1999). Therefore, the solution of Eq. (1) along with assumption (iii) seems unable to account for mixing phenomena arising from lateral and forward velocity fluctuations occurring at small distances from the entrance of the porous medium. Then, the convective–dispersion equation may be written in its more generalized form

$$\frac{\partial C}{\partial t} + \frac{\partial (u_x C)}{\partial x} + \frac{\partial (u_y C)}{\partial y} = D_L \frac{\partial^2 C}{\partial x^2} + D_T \frac{\partial^2 C}{\partial y^2} \quad (23)$$

which can be solved numerically in conjunction with Eqs. (20) and (21). Nevertheless, solute concentrations are measured on a central region

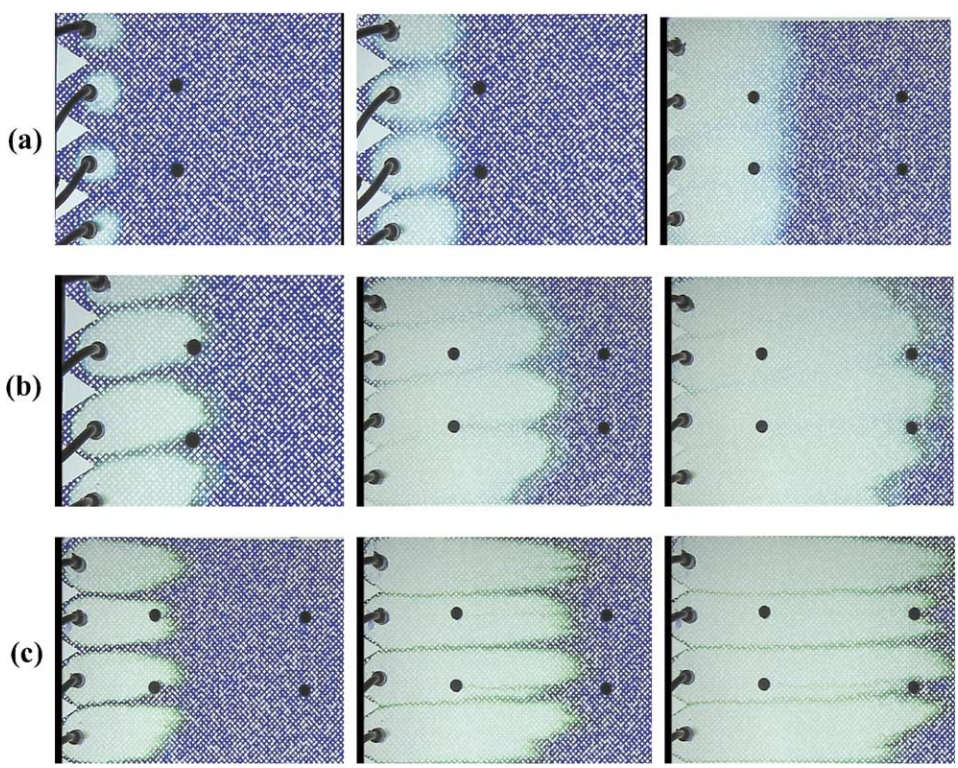

Fig. 7. Successive macroscopic images of miscible displacement experiments. (a) $Pe = 3.0$ (b) $Pe = 30.0$. (c) $Pe = 200.0$.

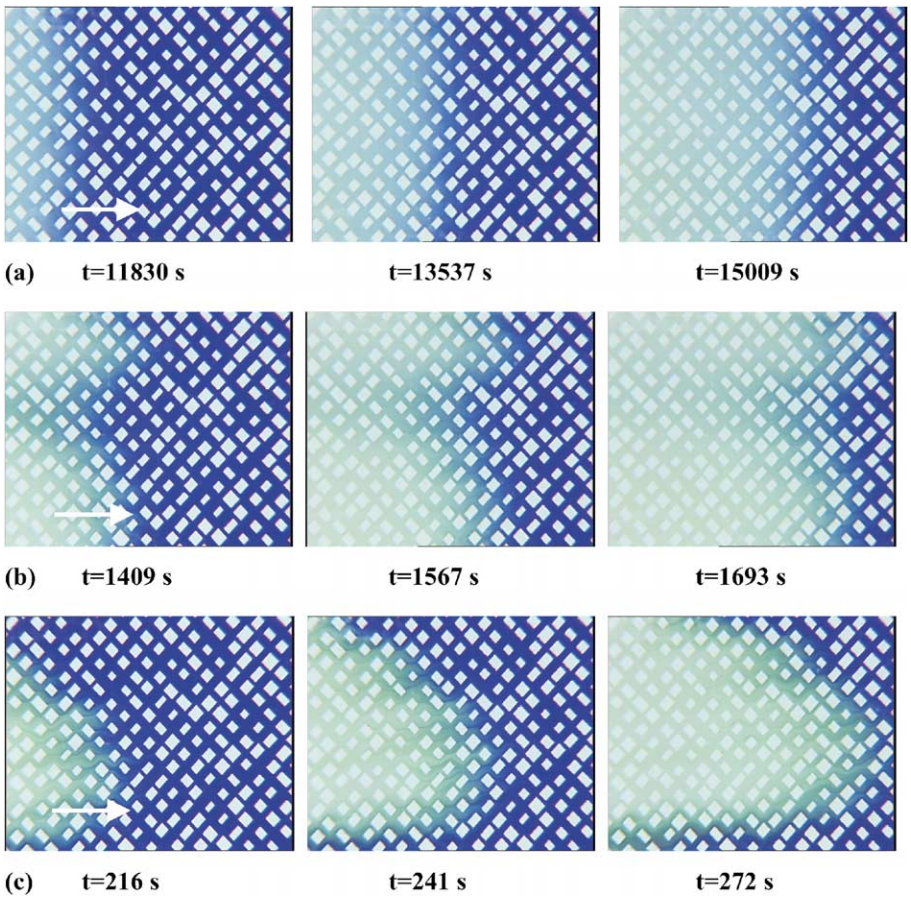

Fig. 8. Successive images of miscible displacement experiments at the observation scale. (a) $Pe = 3.0$. (b) $Pe = 30.0$. (c) $Pe = 200.0$.

of the pore network far from its entrance (Fig. 2b), where $u_x = u_\infty$ and $u_y \cong 0$ (Fig. 6a and b). Hence, an approximate analytical model of the miscible displacement experiments can be obtained by treating them as multi-source-solute transport processes (Fig. 5b). Of course, deviations from the accurate numerical solution of Eq. (23) are unavoidable, since the process is transient, and dispersion history is 'transferred' in the measured solute concentration distribution. However, the numerical solution of Eq. (23) in conjunction with detailed boundary conditions is out of the scope of the present work and is left for a forthcoming publication.

In miscible displacement experiments (Fig. 5b), we assume that $0 < u_0 \leq u_\infty$ and four uniform solute fluxes, F_m, approximated by

$$F_m = \frac{Q(C_0 - C_i)}{4BL_P} \tag{24}$$

are imposed across the inlet ports ($x = 0$). It should be noted that the vertical dimension of the 2D porous medium is selected equal to L_P. The integrals I_0 and I_n are given by

$$I_0 = 4B\frac{F_m}{\varphi} \tag{25}$$

and

$$I_n = \left(\frac{W}{n\pi}\right)\frac{F_m}{\phi}A_n \tag{26}$$

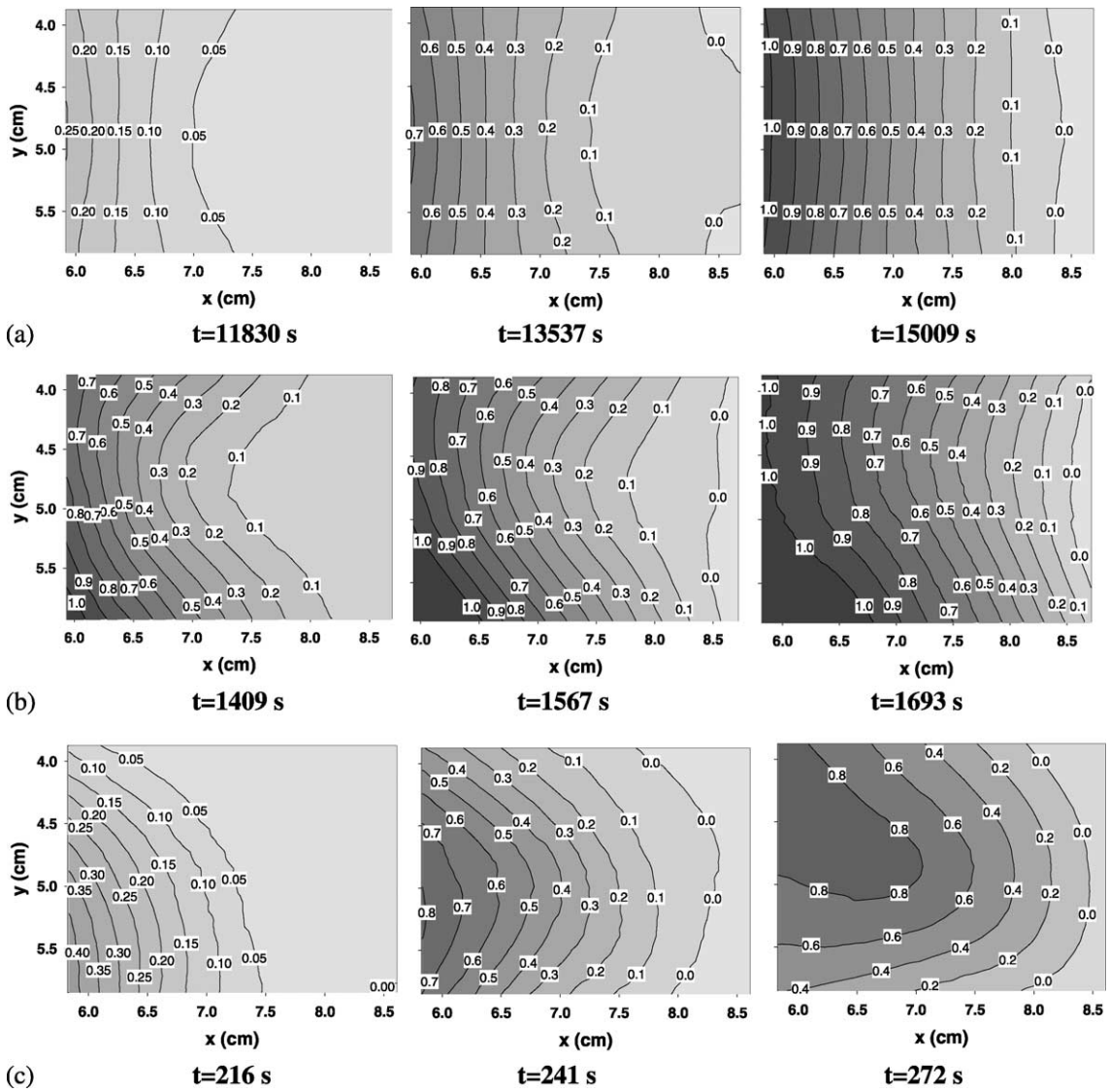

Fig. 9. Contours of equal dimensionless solute concentration, C^*, for the images of Fig. 8. (a) $Pe = 3.0$, (b) $Pe = 30.0$, (c) $Pe = 200.0$.

respectively, whereas the porosity, ϕ, is defined by

$$\phi = \frac{\pi \langle W_P \rangle \langle D_P \rangle}{4L_P^2} \tag{27}$$

It is worthwhile noting that Eq. (24) is derived from Eq. (5) by neglecting the dispersive term at the sources.

For the single source-solute transport experiments (Fig. 5d), the mean pore velocity, u_0, and solute flux, F_m, are given by the relations

$$u_0 = u_\infty \tag{28}$$

and

$$F_m = \frac{Q_s(C_0 - C_i)}{BL_P} \tag{29}$$

respectively, whereas the integrals I_0, I_n are given by

$$I_0 = B\frac{F_m}{\varphi} \tag{30}$$

$$I_n = \frac{2}{\pi n}\frac{F_m}{\varphi}\{\sin[\lambda_n(D_1 + B)] - \sin(\lambda_n D_1)\}. \quad (31)$$

4. Results and discussion

4.1. Miscible displacement experiments

Miscible displacement experiments were performed on the artificial model M-2 (Fig. 1) and the transient variation of the solute concentration was measured on the unit cells of a small region (dimensions ~ 30 mm × 23 mm) on the centre of the pore network (Fig. 2b). The Peclet number is defined by

$$Pe = \frac{u_\infty L_P}{D_m} \quad (32)$$

where D_m is the solute diffusion coefficient in the solvent. For the system HCl–H_2O, D_m was calculated as a function of the HCl concentration (Reid et al., 1977) and its mean value was estimated and found equal to 3.3×10^{-9} m^2/s at 25 °C for the concentration range used in experiments.

The Peclet number expresses roughly the ratio of the diffusion time (required for solute molecules to move from one streamline to another one) to the convection time (required for molecules to move along streamlines at the mean fluid velocity). At relatively low *Pe* values, the diffusion time is comparable to the convection time, and gradually a uniform solute concentration front is established within a small distance from the inlet ports (Fig. 7a). At increasing values of *Pe*, the diffusion time exceeds the convection time, so that the forward convective transport of solute is favoured against its diffusion and lateral transport. In this manner, the macroscopic dispersion pattern consists of four mixing zones, which progressively may coalesce in a non-uniform front, depending on *Pe* value (Fig. 7b). At high *Pe* values, the forward convective dispersion dominates over the lateral one, and separate dispersion pathways (channelling) appear at the macroscopic scale (Fig. 7c).

Analogous dispersion regimes are identified (Fig. 8) and quantified (Fig. 9) at the local observation scale. At low *Pe* values, the time scale for the lateral dispersion of solute is comparable to that for its forward dispersion, and a frontal mixing zone arises (Figs. 8a and 9a). At intermediate *Pe* values, the spatial deviation of the local pore velocity from its average value is greater along the flow direction rather than perpendicular to that, and the mixing zones originating from the corresponding solute sources result in non-uniform solute concentration profiles (Figs. 8b and 9b). At sufficiently high *Pe* values, solute transport along high velocity streamlines is favoured, and channelling, which is characterized by

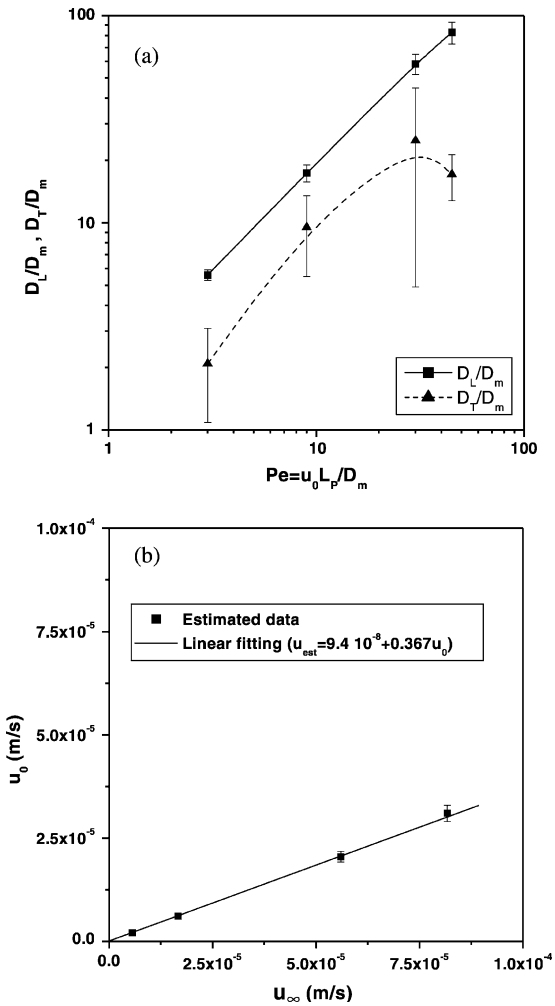

Fig. 10. (a) Longitudinal and transverse dispersion coefficients estimated by fitting the analytic model of Eq. (6) to transient data of miscible displacement experiments. (b) Estimated mean pore velocity as a function of its real asymptotic value.

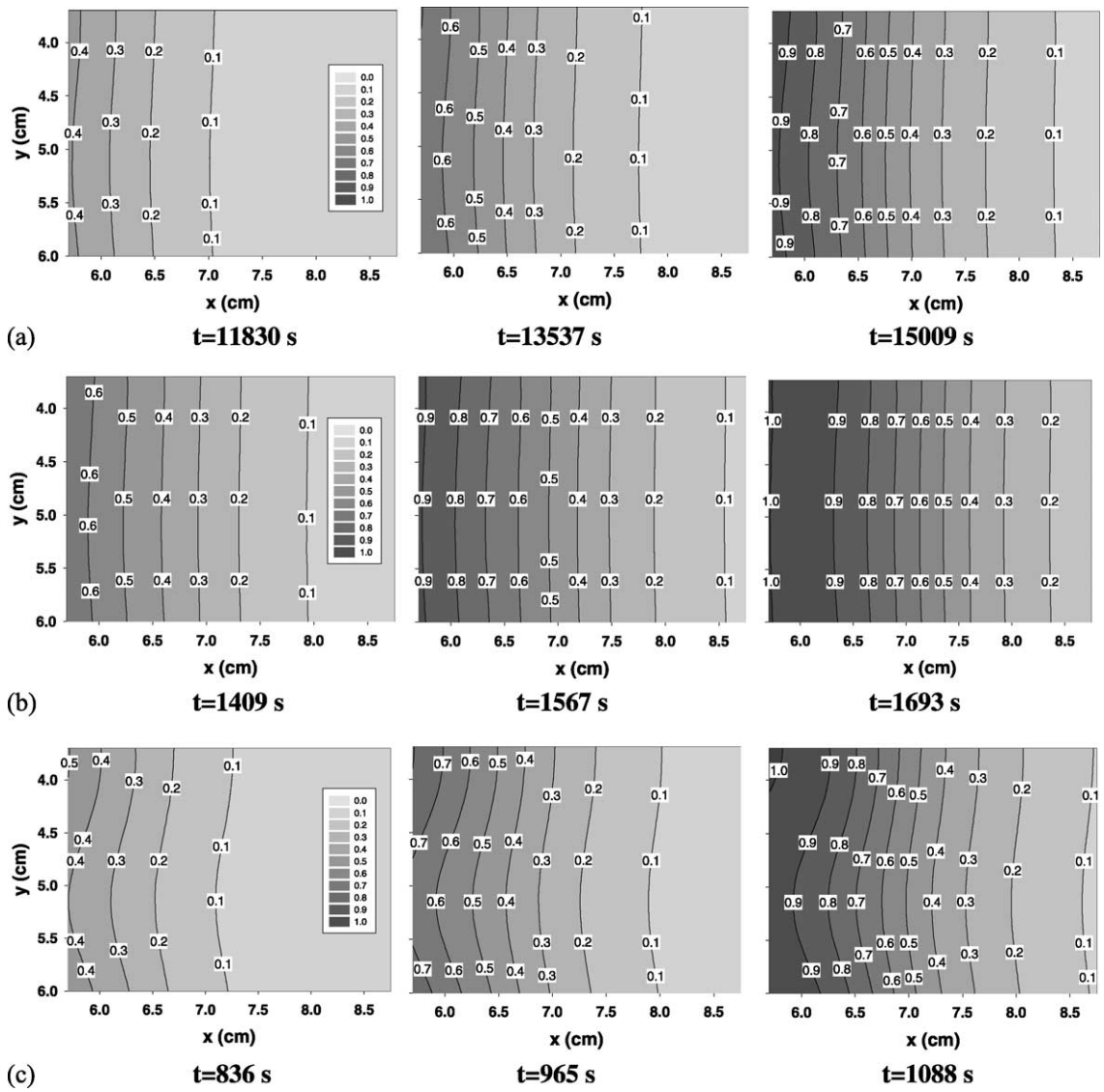

Fig. 11. Contours of equal dimensionless solute concentration, C^*, predicted by Eq. (6) for the parameter values of Fig. 10a. (a) $Pe = 3.0$. (b) $Pe = 30.0$. (c) $Pe = 45.0$.

high local concentration gradients, appears (Figs. 8c and 9c).

The parameter values of D_L, D_T, and u_0 were estimated by fitting transient experimental data (Fig. 9) to the analytic solution, Eq. (6), with the use of the Bayesian estimator of GREGPLUS solver of ATHENA visual workbench package (Stewart and Associates, Inc., USA). In this code, the objective function, a weighted sum of squares of deviations of model predictions from observations, is expanded as a quadratic function of the parameters, around the initial values of the current iteration. The resulting parameter minimization problem is solved with quadratic programming by using a modified Gauss–Jordan algorithm (Bard, 1974). Interval estimates of the parameters are

computed by using a posterior density function constructed from the final quadratic expansion of the objective function (Stewart et al., 1992). The following geometrical properties of the model M-2 (Fig. 5a and b) were used: $D_1 = 1.05$ cm, $D_2 = 3.55$ cm, $D_3 = 6.25$ cm, $D_4 = 8.65$ cm, $B = 0.5$ cm.

We were unable to estimate the dispersion coefficients at high Pe values (Fig. 10a). At $Pe \geq$

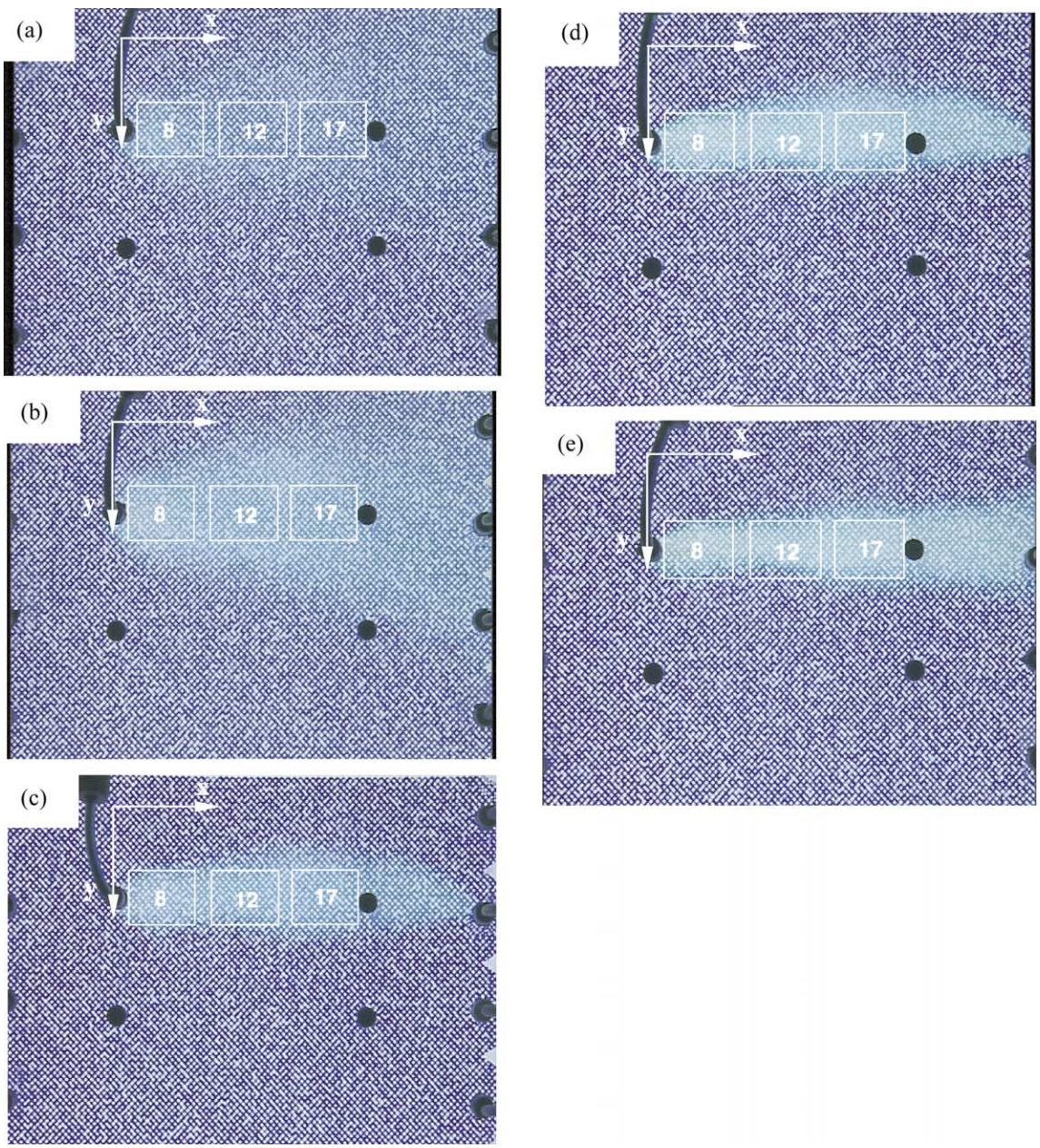

Fig. 12. Macroscopic steady-state dispersion regimes for single source-solute transport experiments performed on model M-1. (a) $Pe = 0.5$. (b) $Pe = 1.0$. (c) $Pe = 2.7$. (d) $Pe = 5.3$. (e) $Pe = 10.6$.

100, the confidence intervals exceeded the mean values of parameters, and therefore the uncertainty embedded into the estimated D_L and D_T values was very high. At high *Pe* values, convective transport dominates, and solute dispersion is affected more drastically by details of the flow field and initial positions of solute molecules (Adler and Thovert, 1999). Consequently, the approximate analytical model, Eq. (6), may fit satisfactorily to experimental solute concentration measurements, at low and intermediate *Pe* values (Fig. 9a and b), but deviates sensibly from observed data at high *Pe* values (Fig. 9c).

D_L follows a power law of the form $D_L \propto Pe^{\beta_L}$ with $\beta_L = 1.006$ (Fig. 10a) and this behaviour is in agreement with earlier experimental results (Sahimi, 1995; Whitaker, 1999). Specifically, at intermediate *Pe* values, macrodispersion induced by the variability of pore sizes dominates, and $D_L \propto Pe$, while at high *Pe* values Taylor dispersion induced by velocity variations across the pore network dominates and $D_L \propto Pe^2$ (Detwiller et al., 2000).

The net flow perpendicular to the main flow direction is nil. However, both horizontal (*x*-axis) and vertical (*y*-axis) components of the spatial deviation of the local pore velocity from its average value arise, because of the angular orientation of pores with respect to the main flow direction, and variability of pore widths (Table 1). In this manner, significant solute dispersion occurs laterally. The transverse dispersion coefficient has the tendency to become constant at increasing *Pe* values (Fig. 10a) in agreement with earlier theoretical studies (Souto and Moyne, 1997). The relatively large confidence intervals of estimated D_T values are associated not only with the simplifying assumptions of the theoretical approach (Fig. 5b) but also with the position of observation area in relation to solute sources (Fig. 2b). At low and intermediate *Pe* values, lateral dispersion of the solute injected through the inlet ports (Fig. 2b) is mostly completed before this area is reached (Fig. 8a and b), quantitative information concerning transverse dispersion at early times is 'lost', and unavoidably the uncertainty embedded into the estimated D_T values is quite high (Fig. 10a).

The estimated mean pore velocity is lower than its asymptotic value and the ratio u_0/u_∞ fits to a straight line with slope ~ 0.36 (Fig. 10b). This difference reflects the approximate nature of the theoretical approach (Fig. 5b), where the problem of solute injection through four inlet ports without pre-existing flow field (Fig. 5a) is regarded equivalent to the multi-source-solute transport problem with constant flow velocity, $u_0 < u_\infty$ (Fig. 5b). At each *Pe* value and for small distances from inlet ports, significant mixing of solutions occurs in the forward and lateral directions, because of strong fluctuations of the local velocities (Fig. 6a and b). Information concerning this mixing step is embedded into the transient concentration profiles, measured at a certain axial distance from inlet ports. The approximate analytical model, Eq. (6), ignores such mixing phenomena, and its fitting to the measurements is interpreted as multi-source solute dispersion in a flow field slower than the real one (Fig. 10b).

The temporal evolution of solute concentrations predicted by the model, Eq. (6), (Fig. 11a and b) are comparable to the corresponding one observed in experiments (Fig. 9a and b). However, at intermediate *Pe* values, the predicted spatial distribution of solute concentration at various times (Fig. 11a and b) is more uniform than the measured one (Fig. 9a and b). This discrepancy is due to the fact that the estimated flow field 'seems' slower than the real one, and the non-uniform distribution of solute concentration along *y*-axis moves to higher *Pe* values (Fig. 11c).

4.2. Single source-solute transport experiments

Single source-solute transport experiments were performed on micromodel M-1. The steady-state dispersion regimes were analysed (Fig. 12a–e) and contours of equal solute concentration were determined (Fig. 13a–e). Steady-state conditions were confirmed by capturing images for a long period after solute breakthrough, until no change was observed between successive shortcuts. At very low *Pe* values, the injected solute is dispersed equally laterally and forwards, and a wide mixing zone of relatively low solute concentrations arises (Figs. 12a and 13a). At increasing *Pe* values, the forward solute dispersion is favoured against the lateral one, the width of the mixing zone is reduced substantially (Fig. 12b–d), and the steady-state solute concentrations increase

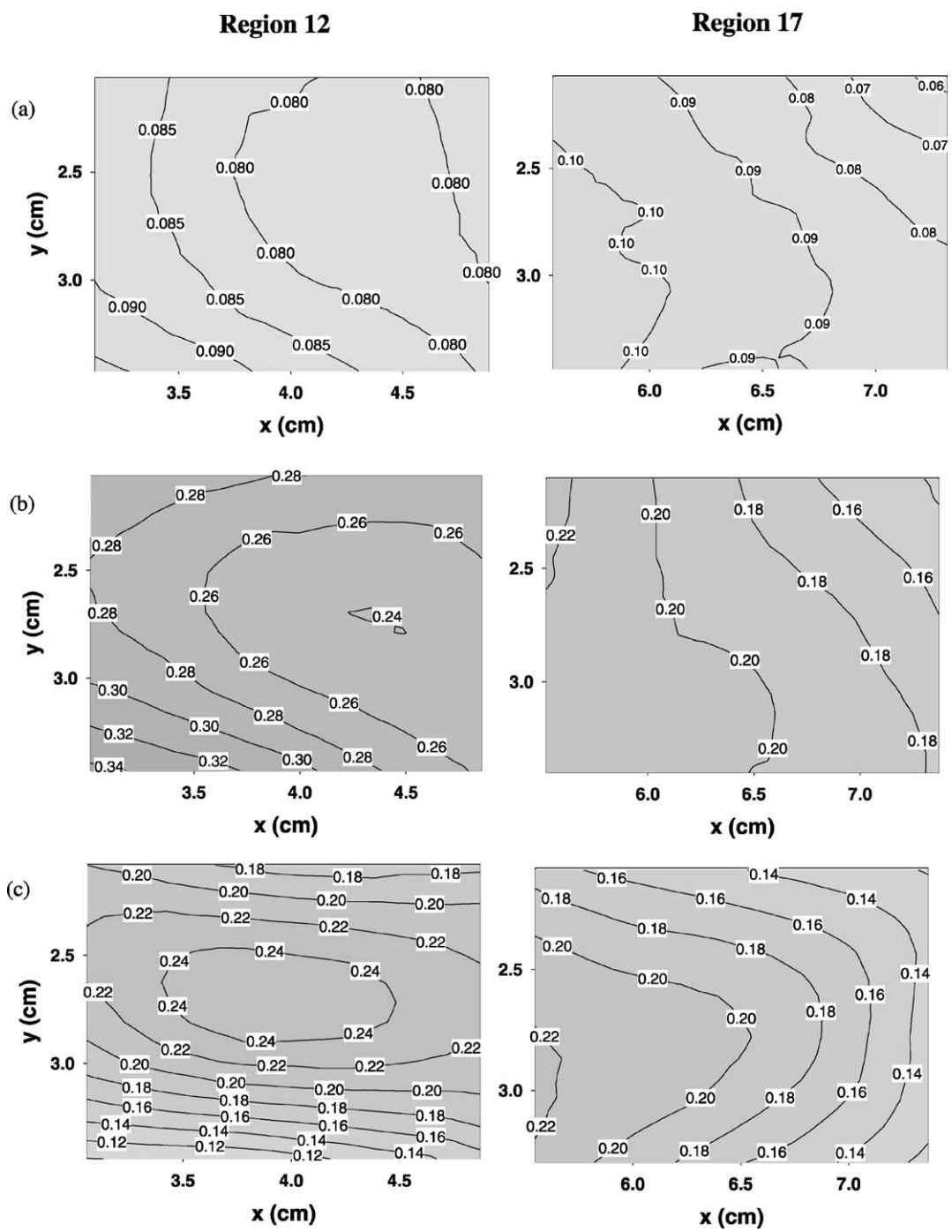

Fig. 13. Contours of equal dimensionless solute concentration, C^*, for two regions of the pore network (Fig. 12). (a) $Pe = 0.5$, (b) $Pe = 1.0$, (c) $Pe = 2.7$, (d) $Pe = 5.3$, (e) $Pe = 10.6$.

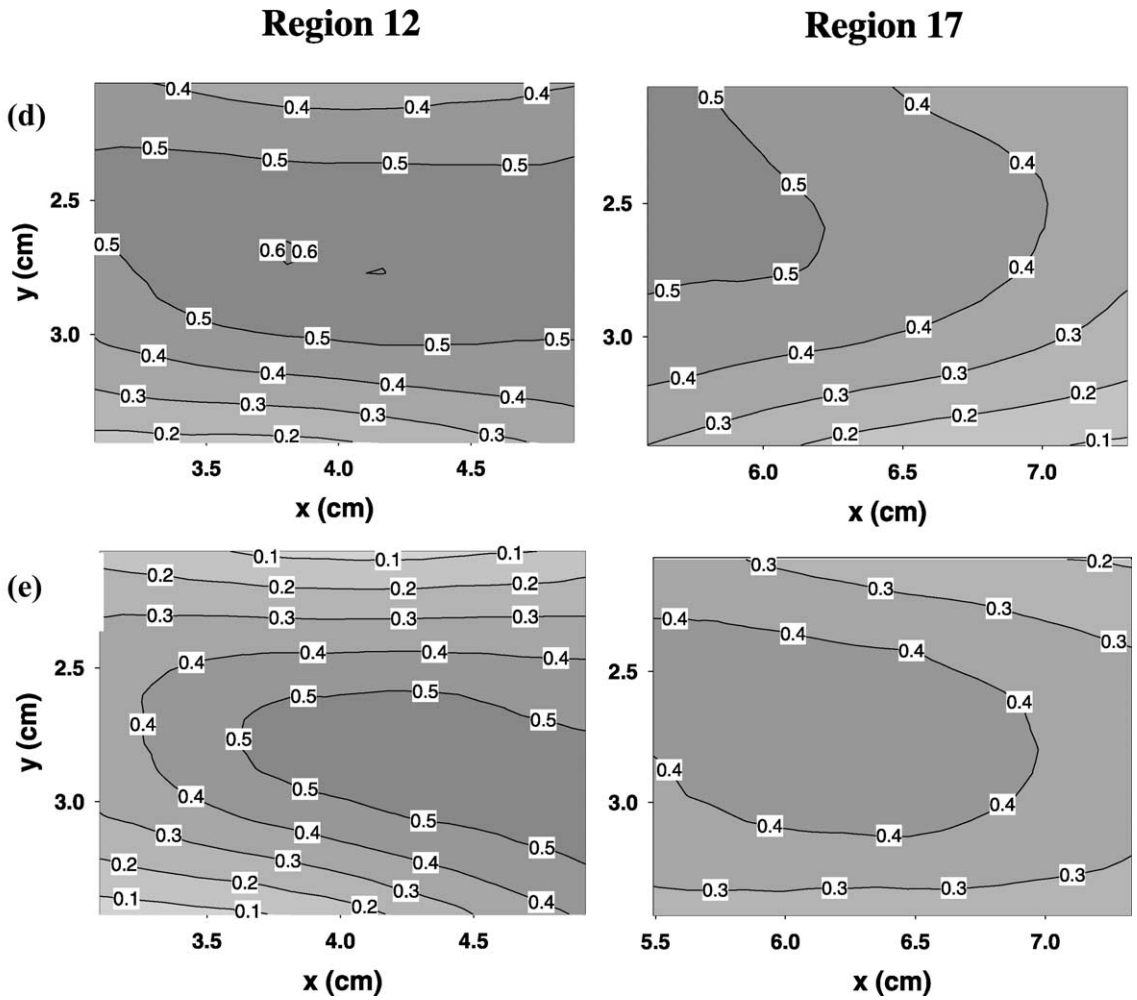

Fig. 13 (*continued*)

(Fig. 13b–d). Progressively, at sufficiently high *Pe* values, dispersion is bounded in a narrow mixing zone with thickness comparable to the source dimensions (Fig. 12e) and the concentration gradients at the vertical direction become quite large (Fig. 13e).

Transient and steady-state short-cuts of dispersion process (Fig. 14) were employed to determine the solute concentration profiles (Fig. 15) which, in turn, were fitted with the analytic model, Eq. (6), to estimate D_L and D_T as functions of Peclet number. Parameter estimation was done by fitting the analytical model, Eq. (6), to the solute concentrations measured on one or two regions of the pore network (regions 12 and 17 in Fig. 12), with the use of ATHENA workbench software package. The following geometrical properties of model M-1 (Fig. 5c and d) were used: $D_1 = 3.5$ cm, $B = 0.5$ cm. In order to reduce the number of experimental data, each region (12 and 17 in Fig. 12) was divided into 5×5 large unit cells composed of a number of elementary cells (Fig. 3a), the solute concentrations were averaged over these large cells, and the reduced solute concentrations were used in parameter estimation.

At early times, the predicted transient solute concentration profiles (Fig. 16a–d) are comparable, in semi-quantitative basis, to corresponding

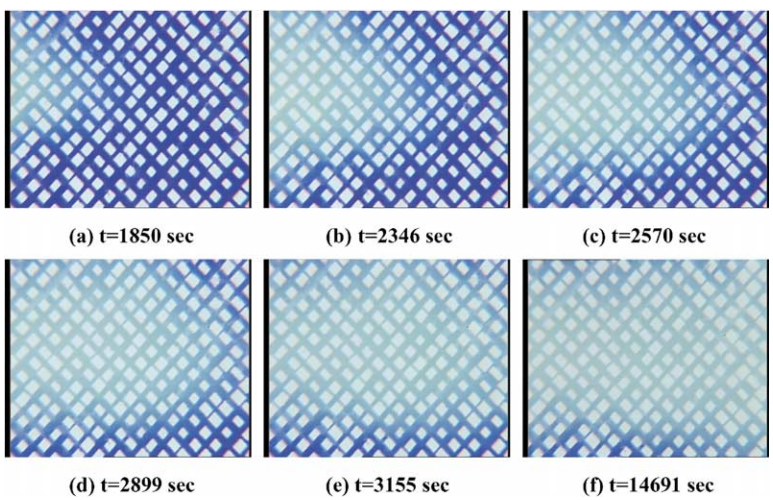

Fig. 14. Successive images of the solute dispersion in region 12 of model M-1 at various times ($Pe = 5.3$); (a–e) transient shortcuts, (f) steady-state short cut.

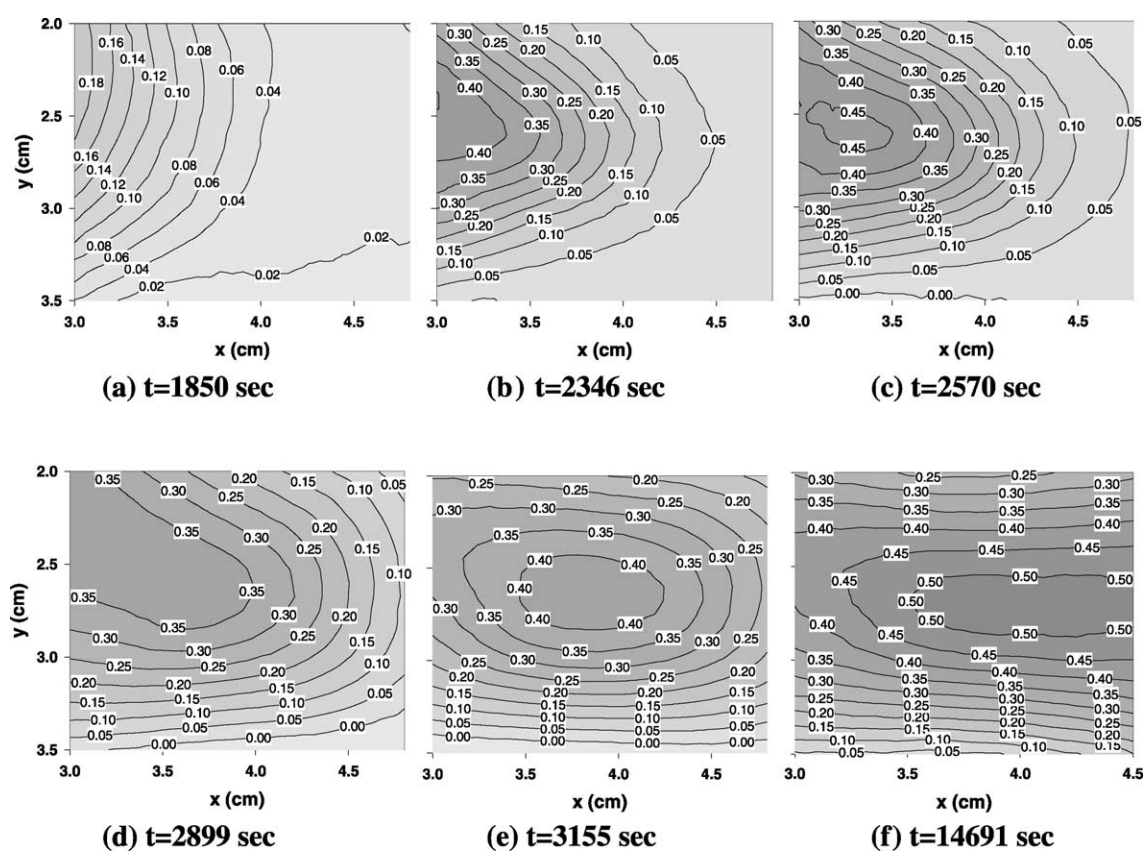

Fig. 15. Contours of equal dimensionless solute concentration, C^*, for the images of Fig. 14 ($Pe = 5.3$); (a–e) transient solute concentration profiles, (f) steady-state solute concentration profiles.

experimental ones (Fig. 15a–d). However, significant differences are observed among them at late times, as steady-state conditions are approached (Figs. 15e and f and 16e and f). The observed discrepancy (Figs. 15e and f and 16e and f) is due to the deviation of the real boundary conditions, prevailing in the pore network exit, from those used in the derivation of theoretical model, Eq. (6). Specifically, the finite length of the experimental porous medium, and existence of four outlet ports of restricted size affects both the flow field and dispersion process.

The estimated parameter values are sensitive to the number of regions used in the fitting procedure. The less the area of the experimental observations, the smaller the difference $D_L - D_T$ and the larger the uncertainty embedded into the values of dispersion coefficients (Fig. 17). D_T is comparable to D_L at very low *Pe* values, takes on a local minimum at a low *Pe* value, and becomes an increasing function of *Pe* at higher values of this parameter (Fig. 17). This behaviour can be explained with reference to the steady-state solute concentration distribution within the pore network (Figs. 12a–e and 13a–e) and using arguments of the volume averaging method as applied to solute dispersion processes (Whitaker, 1999). The total dispersion tensor can be considered as sum of the effective diffusivity and hydrodynamic dispersion tensor defined by (Whitaker, 1999)

$$\mathbf{D} = -\langle \tilde{\mathbf{u}} \cdot \tilde{C} \cdot |\nabla \langle C \rangle|^{-1} \rangle \tag{33}$$

where $\tilde{\mathbf{u}}$, $\tilde{C}$ are the spatial deviations of velocity vector and solute concentration from their intrinsic average values, $\langle \mathbf{u} \rangle$ and $\langle C \rangle$, respectively. For uni-directional steady flow, the order of magnitude of the right-hand side of Eq. (33) is $O(\langle u \rangle \langle C \rangle L_p / \Delta \langle C \rangle_i)$ where $\Delta \langle C \rangle_i$ denotes the average concentration difference along

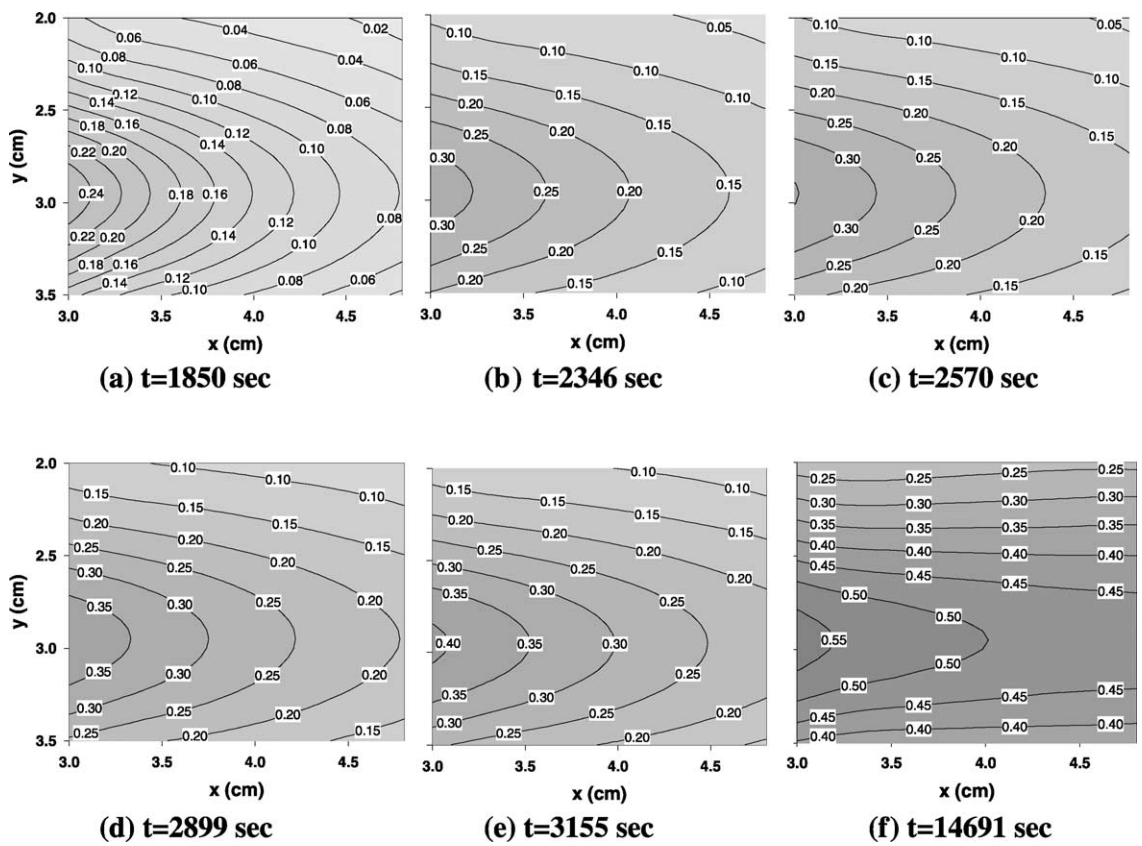

Fig. 16. Contours of equal dimensionless solute concentration, C^*, predicted by the analytic model of Eq. (6), for the estimated parameter values $D_L/D_m = 39.4$ and $D_T/D_m = 2.44$ ($Pe = 5.3$); (a–f) transient solute concentration profiles.

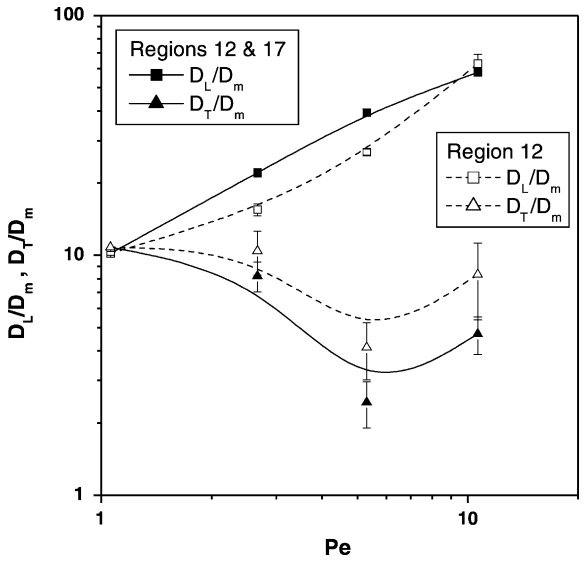

Fig. 17. Longitudinal and transverse dispersion coefficients estimated by fitting the analytic model of Eq. (6) to transient and steady-state data of single source-solute transport experiments.

the i direction and over the length of one unit cell. At increasing $\langle \mathbf{u} \rangle$ values, the forward solute concentration difference $\Delta\langle C \rangle_x$ does not change sensibly, while the lateral component, $\Delta\langle C \rangle_y$ increases (Fig. 13a–e). In this manner, D_L is always an increasing function of Pe, while D_T is a decreasing or increasing function of Pe depending on the relative magnitudes of $\langle u \rangle$ and $\Delta\langle C \rangle_y$ (Fig. 17).

5. Conclusions

A new technique is developed for performing visualization experiments of the hydrodynamic solute dispersion on transparent model porous media. The technique is based on the use of image analysis for the measurement of the colour intensity variation caused on a low solute concentration solution, occupying initially the porous medium, during its mixing with a high solute concentration solution that is injected in the medium through a single or multiple sources. The colour of the solution changes sharply even for a small variation in solute concentration, because of the high sensitivity of a mixture of indicators, contained in traces in both solutions, to pH. Colour intensity–solute concentration calibration curves are constructed from images of the porous medium filled with standard solutions of known concentrations. A code developed in the environment of the image analysis software allows the automatic and accurate measurement of the solute concentration distribution over various regions of the pore network. A generalized analytic solution of the macroscopic convection–dispersion equation, obtained for solute transport from multiple sources in a porous medium, is used for the estimation of the dispersion coefficients. Miscible displacement and single source-solute transport experiments are performed on two glass-etched planar pore networks, and the macroscopic transient and steady-state solute dispersion regimes are correlated with the dominant transport mechanisms. Non-linear fitting of the transient and steady-state solute concentration profiles to analytic solutions of the convection–dispersion equation allows the estimation of the longitudinal and transverse dispersion coefficients as functions of Peclet number. The most important conclusions are outlined below.

- The new technique allows the accurate measurement of solute concentrations and identification of solute dispersion regimes in a pore network.
- The transient dispersion regime changes from an almost uniform front at low Pe values to a non-uniform solute concentration profile at intermediate Pe values, and a channelized pattern at high Pe values.
- Over intermediate Pe values (which are the most common in practical applications) the longitudinal dispersion coefficient follows a power law with exponent equal to 1.
- The transverse dispersion coefficient is an increasing function of Pe and has the tendency to become constant at high Pe values. At low Pe values, the transverse dispersion coefficient may take on a local minimum as the spatial deviation of the local pore velocity and solute concentration from their average values counterbalance each other.
- In single source-solute transport processes, at increasing Pe values, the steady-state dispersion regime changes from a very wide zone of small solute concentrations to a very thin zone of high solute concentrations.

- The new technique is very useful for (i) investigating pollutant dispersion in homogeneous and heterogeneous pore structures of well-controlled morphology under various scenarios of contamination, (ii) providing reliable data for the validation of network-scale and macroscopic-scale numerical simulators of hydrodynamic dispersion, (iii) determine the longitudinal and transverse dispersion coefficients as functions of the pore structure parameters and Peclet number.

Acknowledgements

This work was performed under Energy Environment and Sustainable Development (EESD) contract number EVK1-CT1999-00013 (project acronym: TRACe-Fracture) supported by the European Commission.

References

Adler, P.M., Thovert, J.-F., 1999. Fractures and Fracture Networks: Theory and Applications of Transport in Porous Media, Kluwer, Dordrecht.

Ahmadi, A., Aigueperse, A., Quintard, M., 2001. Calculation of the effective properties describing active dispersion in porous media: from simple to complex unit cells. Adv. Water Resour. 24, 423–438.

de Arcangelis, L., Koplik, J., Redner, S., Wilkinson, D., 1986. Hydrodynamic dispersion in network models of porous media. Phys. Rev. Lett. 57, 996–999.

Aris, R., 1956. On the dispersion of a solute in a fluid flowing through a tube. Proc. R. Soc. Lond. A235, 67–77.

Bacri, J.-C., Rakotomalala, N., Salin, D., 1987. Experimental evidence of disorder effects in hydrodynamic dispersion. Phys. Rev. Lett. 58, 2035–2038.

Bard, Y., 1974. Nonlinear Parameter Estimation, Academic Press, London.

Batu, V., 1993. A generalized two-dimensional analytical solute transport model in bounded media for flux type finite multiple sources. Water Resour. Res. 29, 2881–2892.

Bear, J., Tsang, C.-F., deMarsily, G., 1993. Flow and Contaminant Transport in Fractured Rock, Academic Press, San Diego, CA.

Birovljev, A., Maloy, K.J., Feder, J., Jossang, T., 1994. Scaling structure of tracer dispersion fronts in porous media. Phys. Rev. E 49, 5431–5437.

Bruderer, C., Bernabe, Y., 2001. Network modelling of dispersion: transition from Taylor dispersion in homogeneous networks to mechanical dispersion in very heterogeneous ones. Water Resour. Res. 37, 897–908.

Charlaix, E., Hulin, J.-P., Leroy, C., Zarconne, C., 1988. Experimental study of tracer dispersion in flow through two-dimensional networks of etched capillaries. J. Phys. D: Appl. Phys. 21, 1727–1732.

Corapcioglu, M.Y., Chowdhury, S., Roosevelt, S.E., 1997. Micromodel visualization and quantification of solute transport in porous media. Water Resour. Res. 33, 2547–2558.

Detwiller, R.L., Rajaram, H., Glass, R.J., 2000. Solute transport in variable-aperture fractures: an investigation of the relative importance of Taylor dispersion and macrodispersion. Water Resour. Res. 36, 1611–1625.

Didierjean, S., Souto, H.P.A., Delannay, R., Moyne, C., 1997. Dispersion in periodic porous media. Experience versus theory for two-dimensional systems. Chem. Engng Sci. 52, 1861–1874.

Ding, A., Candela, D., 1996. Probing non-local tracer dispersion in flows through porous media. Phys. Rev. E 54, 656–660.

Drazer, G., Koplik, J., 2001. Tracer dispersion in two-dimensional rough fractures. Phys. Rev. E 63, 056104/1-11.

Drazer, G., Chertcoff, R., Bruno, L., Rosen, M., Hulin, J.P., 1999. Tracer dispersion in packings of porous activated carbon grains. Chem. Engng Sci. 54, 4137–4144.

Huseby, O., Thovert, J.-F., Adler, P.M., 2001. Dispersion in three-dimensional fracture networks. Phys. Fluids 13, 594–615.

Johns, R.A., Roberts, P.V., 1991. A solute transport model for channelized flow in a fracture. Water Resour. Res. 27, 1797–1808.

Keller, A.A., Blunt, M., Roberts, P.V., 1998. Effect of fracture aperture variations on the dispersion of contaminants. Water Resour. Res. 35, 55–63.

Klint, K.E., Tsakiroglou, C.D., 2000. A new method of fracture aperture characterization. In: Tsihrintzis, V.A., (Ed.), Proceedings of the Protection and Restoration of the Environment V, Thassos Island, Greece, vol. 1., pp. 127–136.

Lowe, C.P., Frenkel, D., 1996. Do hydrodynamic dispersion coefficients exist? Phys. Rev. Lett. 77, 4552–4555.

Maloy, K.J., Feder, J., Boger, F., Jossang, T., 1988. Fractal structure of hydrodynamic dispersion in porous media. Phys. Rev. Lett. 61, 2925–2928.

Manz, B., Alexander, P., Gladen, L.F., 1999. Correlations between dispersion and structure in porous media probed by nuclear magnetic resonance. Phys. Fluids 11, 259–267.

Martys, N.S., 1994. Fractal growth in hydrodynamic dispersion through random porous media. Phys. Rev. E 50, 335–342.

Neretnieks, I., Eriksen, T., Tahtinen, P., 1982. Tracer movement in a single fracture in granite rock: some experimental results and their interpretation. Water Resour. Res. 18, 849–858.

Oppenheimer, S.F., 2000. A convection-diffusion problem in a network. Appl. Math. Comp. 112, 223–240.

Peters, E.J., Gharbi, R., Afzal, N., 1996. A look at dispersion in porous media through computed tomography imaging. J. Petr. Sci. Engng 15, 23–31.

Reid, R.C., Prausnitz, J.M., Sherwood, T.K., 1977. The Properties of Gases and Liquids, McGraw-Hill, New York.

Robinson, R.A., Stokes, R.H., 1970. Electrolyte Solutions, Butterworths, London.

Sahimi, M., 1995. Flow and Transport in Porous Media and Fractured Rock: From Classical Methods to Modern Approaches, VCH, Weinheim.

Sahimi, M., Hughes, B.D., Scriven, L.E., Davis, H.T., 1986. Dispersion in flow through porous media—I. One-phase flow. Chem. Engng Sci. 41, 2103–2122.

Shapiro, A.M., Nicholas, J.R., 1989. Assessing the validity of the channel model of fracture aperture under field conditions. Water Resour. Res. 25, 817–828.

Souto, H.P.A., Moyne, C., 1997. Dispersion in two-dimensional periodic porous media. Part II. Dispersion tensor. Phys. Fluids 9, 2253–2263.

Stewart, W., Caracotsios, M., Sorensen, J.P., 1992. Parameter estimation from multiresponse data. AIChE J. 38, 641–650.

Taylor, G.I., 1953. Dispersion of soluble matter in solvent flowing slowly through a tube. Proc. R. Soc. Lond. A219, 186–203.

Theodoropoulou, M., Karoutsos, V., Tsakiroglou, C., 2001. Investigation of the contamination of fractured formations by non-Newtonian oil pollutants. J. Environ. Forensics 2, 321–333.

Tsakiroglou, C.D., Payatakes, A.C., 1998. Mercury intrusion and retraction in model porous media. Adv. Colloid Interface Sci. 75, 215–253.

Tsakiroglou, C.D., Kolonis, G.B., Roumeliotis, T.C., Payatakes, A.C., 1997. Mercury penetration and snap-off in lenticular pores. J. Colloid Interface Sci. 193, 259–272.

Whitaker, S., 1999. The Method of Volume Averaging, Kluwer, Dordrecht.